Bistability of liquid crystal microcavities

G. D'Alessandro and A. A. Wheeler

Department of Mathematics, University of Southampton, Southampton, SO17 1BJ, United Kingdom
(Received 4 October 2002; published 28 February 2003)

We develop a model of a liquid crystal Fabry-Pérot microcavity. We study the homeotropic and the hybrid cavity configurations and show that both are multistable. Moreover, in the hybrid case a branch of solutions disconnected from the zero field solution exists.

I. INTRODUCTION

Liquid crystals are in many respects ideal components for experiments in nonlinear optics: their large effective nonlinearity and slow time scale imply that complex bifurcations and behaviors can be observed at relatively low powers and detected with relatively inexpensive equipment. Of course, the slow time scale has the drawback that liquid crystals are too slow for many applications (see Ref. [1] for a survey of a recent collaboration to develop liquid crystal based optical devices). However, the rich dynamics of liquid crystals, which may involve optical and thermal nonlinearities together with fluid motion, has been a fertile test bed for many experiments and theoretical models. For example, various experiments [2–5] have detected filamentation and soliton formation during propagation of laser beams in liquid crystals. From the theoretical side, models of the formation and evolution of filaments have been developed in Refs. [6,7], the propagation of beams has been investigated in Refs. [8–10], while the interplay between optical nonlinearities and fluid motion has been discussed in Ref. [11]. Moreover, it has long been known [12] that cavities filled with liquid crystals are multistable and that thermal and optical nonlinearities may both be at play in shaping their dynamics. The bistability is caused by the dispersive properties of the liquid crystal that acts in a very similar way to the sodium vapor in the cavities analyzed in Refs. [13,14].

Here we develop and analyze a model of a planar microcavity filled with a nematic liquid crystal, such as the one used in the experiments of Ref. [12] and Ref. [15]. This device, illustrated schematically in Fig. 1, consists of a thin cavity of length L of the order of 100 light wavelengths entirely filled with a nematic liquid crystal. In the experiment of Ref. [12] the cavity is homeotropic, i.e., the director field on both sides of the cavity is orthogonal to the mirrors. In the experiment of Ref. [15] the cavity is hybrid: the director field is orthogonal to the left mirror and parallel to the other. The model we derive here is for generic boundary conditions on the director field. We discuss at length in Secs. III B and III C the difference between the hybrid and homeotropic cases. A linearly polarized light beam of amplitude F_{in} and frequency ω is injected in the cavity and the intensity I_{out} of the field leaking out from the right-hand mirror is measured. In particular, in the experiment of Ref. [15] it was observed that the cavity is multistable and is able to switch from a uniform low-power state to a patterned high-power output. Apart from the simple model introduced in Ref. [12] and

subsequently used in Refs. [16,17], we are not aware of the existence of a detailed model of this device nor of any theoretical prediction of this behavior. In the following section we develop a model for the cavity of Fig. 1 under the assumption that fluid motion and thermal effects are not significant, i.e., that the power of the intracavity laser field is sufficiently small. This hypothesis is consistent with the results of Ref. [15] and with the low-power results of Ref. [12]. In Sec. III we restrict our attention to the purely longitudinal case and show that the cavity is multistable. The analytical and numerical study of the model with transverse effect will be discussed in a future paper.

II. THE MODEL

We choose a coordinate system as in Fig. 1: the x_3 axis is parallel to the cavity axis and the x_1 axis is parallel to the polarization of the input beam. Moreover, we assume that the director field at the boundaries has no component in the x_2 direction. This implies that neither the electric nor the director field have components in the x_2 direction anywhere in the cavity.

The derivation of the model comprises a number of steps. We first derive the equation of propagation of an electromagnetic wave through a liquid crystal. This is subsequently extended to the case of two counterpropagating waves. We then derive an equation for the director field and, finally, we couple all the equations together and introduce convenient nondimensional variables.

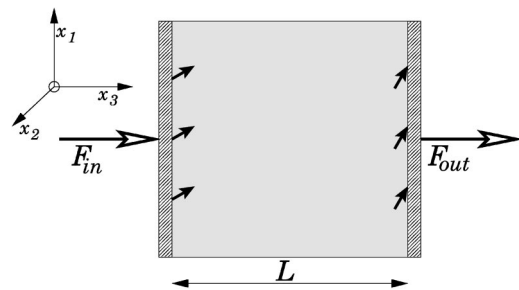The evolution of the electromagnetic field is given by

FIG. 1. Schematic diagram of the liquid crystal filled microcavity analyzed in this paper. The liquid crystal director field, indicated by the small arrows in the diagram, is anchored at given angles on the two sides of the cavity. A light beam of amplitude F_{in} is injected in the left-hand side of the cavity. F_{out} is the amplitude of the field exiting from the right-hand side of the cavity.

Maxwell's equations in a medium [18] without free charges and currents:

$$\nabla \cdot \boldsymbol{D} = 0, \quad \nabla \cdot \boldsymbol{B} = 0,$$

$$\nabla \times \boldsymbol{E} + \frac{\partial \boldsymbol{B}}{\partial t} = 0, \quad \nabla \times \boldsymbol{H} = \frac{\partial \boldsymbol{D}}{\partial t}, \tag{1}$$

where $\boldsymbol{E}$ and $\boldsymbol{B}$ are, respectively, the electric and magnetic fields. The liquid crystals can be considered magnetically inactive so that the induction field $\boldsymbol{H}$ is $\boldsymbol{H} = \boldsymbol{B}/\mu_0$, with μ_0 the vacuum magnetic permeability. The electric displacement field is given by [6]

$$D_j = \varepsilon_0 \varepsilon_\perp \varepsilon_{jk} E_k, \tag{2}$$

where we have used Einstein's convention of summing on repeated indexes and we have indicated the components of a generic vector $\boldsymbol{v}$ as (v_1, v_2, v_3). Here ε_0 is the vacuum dielectric constant and $\varepsilon_\perp$ is the relative dielectric constant of the liquid crystal for an optical field polarized orthogonal to the orientation of the molecules. We represent the orientation of the molecules of the liquid crystal using a unit vector $\boldsymbol{n}$. The tensor ε_{jk} is related to the orientation vector by

$$\varepsilon_{jk} = \delta_{jk} + \alpha n_j n_k, \tag{3}$$

where δ_{jk} is Kronecker's delta and α is a dimensionless measure of the birefringence of the liquid crystal at optical frequencies,

$$\alpha = \frac{\varepsilon_\parallel - \varepsilon_\perp}{\varepsilon_\perp}, \tag{4}$$

with $\varepsilon_\parallel$ the relative dielectric constant for an optical field parallel to the crystal molecules.

Maxwell's equations (1) can be recast as a wave equation using Eq. (2). Its expression in components is:

$$\alpha \partial_q \partial_j (n_j n_p E_p) + \partial_j \partial_j E_q = \frac{1}{v_\perp^2} \partial_{tt} E_q + \frac{\alpha}{v_\perp^2} \partial_{tt}(n_q n_p E_p),$$

$$q = 1,2,3, \tag{5}$$

where ∂_q is the partial derivative with respect to x_q, ∂_{tt} is the second derivative with respect to time, $v_\perp^2 = c^2/\varepsilon_\perp$, and c is the speed of light in vacuum.

In order to simplify Eq. (5) we assume that α is a small parameter. From Eq. (5) we see that the electric field can be written as a wave, solution of Eq. (5) with $\alpha = 0$, whose amplitude is modulated on a space and time scale of the order of $1/\alpha$. We can therefore make use of the slowly varying amplitude approximation and write the electric field as

$$E_q = \frac{1}{2} A_q(\bar{\boldsymbol{x}}, \bar{\bar{\boldsymbol{x}}}, \ldots, t, \bar{t}, \bar{\bar{t}}, \ldots) e^{i(kx_3 - \omega t)} + \text{c.c.}$$

$$+ \frac{\alpha}{2} \overline{A_q}(\bar{\boldsymbol{x}}, \bar{\bar{\boldsymbol{x}}}, \ldots, t, \bar{t}, \bar{\bar{t}}, \ldots) e^{i(kx_3 - \omega t)} + \text{c.c.}$$

$$+ \frac{\alpha^2}{2} \overline{\overline{A_q}}(\bar{\boldsymbol{x}}, \bar{\bar{\boldsymbol{x}}}, \ldots, t, \bar{t}, \bar{\bar{t}}, \ldots) e^{i(kx_3 - \omega t)} + \text{c.c.}$$

$$+ O(\alpha^3), \quad q = 1,3, \tag{6}$$

where $\boldsymbol{x}$ is a compact notation for the three spatial coordinates, ω is the frequency of the injected beam, and k is a wave number whose value is fixed later on when expanding the wave equation (5) in powers of the small parameter $\alpha \ll 1$. The number of overbars indicates the order in α: for example, $\bar{\boldsymbol{x}} \equiv \alpha \boldsymbol{x}$ and $\bar{\bar{\boldsymbol{x}}} \equiv \alpha^2 \boldsymbol{x}$. As the director field is modulated by the amplitude of the electric field we can also assume that its components are functions of the slow space and time variables,

$$n_q = n_q(\bar{\boldsymbol{x}}, \bar{t}, \ldots). \tag{7}$$

The derivation of the field propagation equation consists in substituting the expressions (6) and (7) in the wave equation (5), collecting different powers of α and ensuring that at all orders the appropriate solvability conditions are satisfied. After rather long algebra one obtains that the wave number k has value $\omega/v_\perp$, that the longitudinal component is of the order of α, i.e., that $A_3 = 0$, and that the transverse component A_1 satisfies, up to order α^2, the equation

$$\frac{1}{v_\perp}\left(1 + \frac{\alpha}{2}n_1^2\right)\frac{\partial}{\partial t}A_1 + \frac{\partial}{\partial x_3}A_1 = i\frac{k\alpha}{2}n_1^2\left[1 - \alpha\left(1 - \frac{3}{4}n_1^2\right)\right]A_1 + \frac{i}{2k}\left(\frac{\partial^2}{\partial x_1^2} + \frac{\partial^2}{\partial x_2^2}\right)A_1 - \frac{\alpha}{2}A_1 n_1\left(\frac{\partial}{\partial x_3} + \frac{3}{v_\perp}\frac{\partial}{\partial t}\right)n_1$$

$$- \frac{\alpha}{2}A_1\frac{\partial}{\partial x_1}(n_1 n_3) - \alpha n_1 n_3\frac{\partial}{\partial x_1}A_1, \tag{8}$$

where all the terms are measurable physical quantities.

The coefficient in front of the time derivative indicates that the phase velocity of the field is equal to $v_\perp$ only if the director field is orthogonal to the electric field, i.e., if $n_1 = 0$. The phase velocity in a medium with uniform director field is given by

$$v = v_\perp \sqrt{\frac{1 + \alpha n_3^2}{1 + \alpha}}. \tag{9}$$

The coefficient in front of the time derivative in Eq. (8) is the first-order expansion of $1/v$ in powers of α. A similar argument explains the first term on the right-hand side of Eq. (8): if $n_1 \neq 0$ the choice of wave number, $k = \omega/v_\perp$, is not appropriate and a phase shift accumulates as the field propagates in the x_3 direction.

We now generalize Eq. (8) to the case of two counter-propagating fields in a cavity with injected signal as in Fig. 1. We let F and B denote the slowly varying amplitudes of the forward and backward fields, respectively. The forward field, is expanded exactly as in Eq. (6). In the case of the backward field the sign of k in the exponential is changed. The equations for the two fields are

$$\frac{1}{v_\perp}\left(1 + \frac{\alpha}{2}n_1^2\right)\frac{\partial}{\partial t}\binom{F}{B} \pm \frac{\partial}{\partial x_3}\binom{F}{B} = i\frac{k\alpha}{2}n_1^2\left[1 - \alpha\left(1 - \frac{3}{4}n_1^2\right)\right]\binom{F}{B} + \frac{i}{2k}\left(\frac{\partial^2}{\partial x_1^2} + \frac{\partial^2}{\partial x_2^2}\right)\binom{F}{B} - \frac{\alpha}{2}\binom{F}{B}n_1\left(\pm\frac{\partial}{\partial x_3} + \frac{3}{v_\perp}\frac{\partial}{\partial t}\right)n_1$$

$$\mp\frac{\alpha}{2}\binom{F}{B}\frac{\partial}{\partial x_1}(n_1 n_3) \mp \alpha n_1 n_3 \frac{\partial}{\partial x_1}\binom{F}{B}, \tag{10}$$

where the top and bottom signs refer to the forward and backward fields, respectively. The boundary conditions on the two fields are

$$F(x_1, x_2, 0, t) = R_L B(x_1, x_2, 0, t) + F_{in},$$

$$B(x_1, x_2, L, t) = R_R e^{i\delta_c} F(x_1, x_2, L, t), \tag{11}$$

where $R_{L,R}$ are the left and right complex mirror reflectance, respectively, and δ_c is the constant director field phase shift, $\delta_c \equiv 2kL \, \mathrm{mod}_{2\pi}$.

The equation for the director field in the presence of an electric field E is [6,19]

$$\gamma_1 \frac{\partial n}{\partial t} = K\nabla^2 n + \mu n + \alpha\varepsilon_0\varepsilon_\perp(n\cdot E)E, \tag{12}$$

where the rotational viscosity γ_1 is proportional to the liquid crystal time constant, the elastic constant K is the liquid crystal diffusion coefficient, and μ is a Lagrange multiplier that ensures that $\|n\| = 1$. In writing Eq. (12) we have neglected backflow (the coupling between the liquid flow and the nematic director) and we have assumed that the one elastic constant approximation holds.

In the configuration of the cavity of Fig. 1 the second component of the director field is zero. We can therefore represent the director field using the angle ϑ between n and the x_3 axis,

$$n = [\sin(\vartheta), 0, \cos(\vartheta)]. \tag{13}$$

This representation automatically satisfies the constraint $\|n\| = 1$, so that Eq. (12) can be written as

$$\gamma_1 \frac{\partial\vartheta}{\partial t} = K\nabla^2\vartheta + \alpha\varepsilon_0\varepsilon_\perp[E_1\sin(\vartheta) + E_3\cos(\vartheta)][E_1\cos(\vartheta)$$

$$- E_3\sin(\vartheta)]. \tag{14}$$

The boundary conditions at the two ends of the cavity are

$$\vartheta(x_1, x_2, 0, t) = \vartheta_L, \quad \vartheta(x_1, x_2, L, t) = \vartheta_R, \tag{15}$$

where $\vartheta_{L,R}$ are, respectively, the anchoring angles of the director field at the left and right ends of the cavity.

The next step in the derivation of the model is to couple the equations for the counter-propagating electric fields (10) with the equation for the director field (14). We start by noticing that the dynamics of the liquid crystal is much slower than that of the electric field. We can therefore introduce two different "times." The electric field evolves according to a nondimensional fast "field time," t_f, defined in terms of the cavity round-trip time τ_C,

$$\tau_C = L/v_\perp, \quad t_f = t/\tau_C, \tag{16}$$

while the director field depends on a nondimensional slow "liquid crystal time," i.e., the rotational diffusion time over a distance L, τ_ℓ:

$$\tau_\ell = \gamma_1 L^2/K, \quad t_\ell = t/\tau_\ell. \tag{17}$$

In particular, this implies that the director field can be considered as a time-independent quantity in the electric-field equations that can be written as

$$\frac{1}{L}\left[1 + \frac{\alpha}{2}\sin^2(\vartheta)\right]\frac{\partial}{\partial t_f}\binom{F}{B} \pm \frac{\partial}{\partial x_3}\binom{F}{B} = i\frac{k\alpha}{2}\sin^2(\vartheta)\left\{1 - \alpha\left[1 - \frac{3}{4}\sin^2(\vartheta)\right]\right\}\binom{F}{B} + \frac{i}{2k}\left(\frac{\partial^2}{\partial x_1^2} + \frac{\partial^2}{\partial x_2^2}\right)\binom{F}{B}$$

$$\mp\frac{\alpha}{4}\sin(2\vartheta)\frac{\partial\vartheta}{\partial x_3}\binom{F}{B} \mp \frac{\alpha}{2}\binom{F}{B}\cos(2\vartheta)\frac{\partial\vartheta}{\partial x_1} \mp \frac{\alpha}{2}\sin(2\vartheta)\frac{\partial}{\partial x_1}\binom{F}{B}. \tag{18}$$

On the other hand, the liquid crystals are too slow to see the effect of the instantaneous electric field. We can therefore interpret the source terms in Eq. (14) as averages over a time scale that is considerably longer than τ_C, but shorter than τ_ℓ.

The second observation is that in the derivation of the electric-field equation we have assumed that α is a small parameter. Applying the same approximation to the director field equation we can neglect the longitudinal components of the electric fields from the source term of Eq. (14), which can be written as

$$\frac{\gamma_1}{\tau_\ell}\frac{\partial\vartheta}{\partial t_\ell}=K\nabla^2\vartheta+\frac{\alpha}{4}\varepsilon_0\varepsilon_\perp\sin(2\vartheta)\langle|F|^2+|B|^2\rangle_{t_f}, \quad (19)$$

where the angular brackets indicate the averaging operation over the time t_f. Moreover, in writing Eq. (19) we have implicitly assumed that the diffusion of the liquid crystal is strong enough that the standing wave pattern $FB^*\exp(i2kx_3)$ of the electric field intensity can be neglected.

Equations (18) and (19) together with the boundary conditions (11) and (15) comprise our model. However, it is convenient to express them in terms of nondimensional variables. We have already introduced two nondimensional time variables. We scale the space variables with the cavity length and introduce

$$x'_q=x_q/L. \quad (20)$$

It is customary to scale the transverse coordinate with a length whose Rayleigh range is the length of the cavity because this is the natural length scale for transverse patterns in a "standard size" cavity [20]. However, the cavity analyzed in this paper is so short in units of the light wavelength that such scaling length turns out to be inappropriate, being much smaller than the diffusion length of the liquid crystal. Using the scaling (20) the electric field equations (18) become

$$\left[1+\frac{\alpha}{2}\sin^2(\vartheta)\right]\frac{\partial}{\partial t_f}\binom{F}{B}\pm\frac{\partial}{\partial x'_3}\binom{F}{B}$$

$$=i\Delta(\vartheta)\binom{F}{B}+ia\nabla_\perp^2\binom{F}{B}\mp\frac{\alpha}{4}\sin(2\vartheta)\frac{\partial\vartheta}{\partial x'_3}\binom{F}{B}$$

$$\mp\frac{\alpha}{2}\binom{F}{B}\cos(2\vartheta)\frac{\partial\vartheta}{\partial x_1}\mp\frac{\alpha}{2}\sin(2\vartheta)\frac{\partial}{\partial x_1}\binom{F}{B}, \quad (21)$$

where $\nabla_\perp^2$ is the Laplacian in the nondimensional transverse coordinates and $a\equiv(2kL)^{-1}$ is the diffraction parameter. The phase shift term $\Delta(\vartheta)$ is given by

$$\Delta(\vartheta)=\frac{\alpha}{4a}\sin^2(\vartheta)\left\{1-\alpha\left[1-\frac{3}{4}\sin^2(\vartheta)\right]\right\}. \quad (22)$$

For a 100 light wavelength long cavity a has value $(400\pi)^{-1}\simeq0.0008$. Typical values of α are of the order of $\alpha\simeq0.1$. These values imply that $\Delta(\vartheta)\sim O(100)$ and its

presence causes the electric fields to oscillate rapidly during propagation. These oscillations may cause considerable numerical problems. It is therefore useful to eliminate the phase-shift term from the field equations by introducing the field variables

$$\binom{f}{b}\equiv\frac{L}{2}\sqrt{\frac{\alpha\varepsilon_0\varepsilon_\perp}{K}}\binom{e^{-i\Phi(x'_3)}F}{e^{+i\Phi(x'_3)}B}, \quad (23)$$

where the phase $\Phi(x'_3)$ is

$$\Phi(x'_3)=\int_0^{x'_3}\Delta(\vartheta)d\zeta. \quad (24)$$

In terms of the new field variables f and b the equations for the electric fields (21) and the director (19) become

$$\left[1+\frac{\alpha}{2}\sin^2(\vartheta)\right]\frac{\partial}{\partial t_f}\binom{f}{b}\pm\frac{\partial}{\partial x'_3}\binom{f}{b}$$

$$=iae^{\mp i\Phi}\nabla_\perp^2e^{\pm i\Phi}\binom{f}{b}\mp\frac{\alpha}{4}\sin(2\vartheta)\frac{\partial\vartheta}{\partial x'_3}\binom{f}{b}$$

$$\mp\frac{\alpha}{2}\binom{f}{b}\cos(2\vartheta)\frac{\partial\vartheta}{\partial x_1}\mp\frac{\alpha}{2}\sin(2\vartheta)$$

$$\times e^{\mp i\Phi}\frac{\partial}{\partial x_1}\left[e^{\pm i\Phi}\binom{f}{b}\right], \quad (25)$$

$$\frac{\partial\vartheta}{\partial t_\ell}=\nabla^2\vartheta+\sin(2\vartheta)\langle|f|^2+|b|^2\rangle_{t_f}. \quad (26)$$

The boundary conditions on these equations can be obtained from Eqs. (11) and (15) in terms of the new variables:

$$f(x'_1,x'_2,0,t_f)=R_Lb(x'_1,x'_2,0,t_f)+f_{in}, \quad (27)$$

$$b(x'_1,x'_2,1,t_f)=R_Re^{i\psi}f(x'_1,x'_2,1,t_f), \quad (28)$$

$$\vartheta(x'_1,x'_2,0,t_\ell)=\vartheta_L, \quad \vartheta(x'_1,x'_2,1,t_\ell)=\vartheta_R, \quad (29)$$

where f_{in} is the scaled input field amplitude,

$$f_{in}=L/2\sqrt{\frac{\alpha\varepsilon_0\varepsilon_\perp}{K}}F_{in}. \quad (30)$$

Using "standard" values for the liquid crystal ($n_\parallel=1.7$, $n_\perp=1.5$, $K=10^{-11}$ N) and for the electromagnetic cavity ($\lambda=780$ nm, $L=57$ μm) we obtain that a field with nondimensional amplitude $f=1$ has power per unit area equal to approximately 4 MW m^{-2}. The phase shift ψ that appear in the boundary condition (28) can be written as

$$\psi=\delta_c+2\Phi(1)=\delta_c+2\int_0^1\Delta(\vartheta)d\zeta. \quad (31)$$

However, the constant director field phase shift δ_c is not a very appropriate physical quantity in this context. It is more convenient to introduce the zero-electric-field phase shift,

$$\delta_e \equiv \delta_c + 2\Delta(\vartheta_0), \qquad (32)$$

where ϑ_0 is the solution of Eq. (26) with $|f| = |b| = 0$. This phase shift has a clear physical meaning: if $\delta_e = 0$ a low (nominally zero) intensity field is resonant with the cavity. In terms of δ_e the total phase shift ψ is

$$\psi = \delta_e + 2\int_0^1 [\Delta(\vartheta) - \Delta(\vartheta_0)]d\zeta. \qquad (33)$$

Equations (25) and (26) together with the boundary conditions (27)–(29) describe the evolution of the electromagnetic field in a liquid crystal cavity and are the main result of this section. They rest on several simplifying hypotheses: (1) fluid motion and thermal effects can be neglected; (2) the slowly varying amplitude approximation can be applied; (3) the electric fields evolve on a much faster time scale than the liquid crystal; and (4) the birefringence parameter α is small.

III. THE PLANE-WAVE LIMIT

A. Derivation of the model

The analysis of the full equations (25) and (26) is in progress and will be reported elsewhere. Here we want to discuss a simpler problem, their plane-wave limit, namely, the case that none of the fields depends on the transverse coordinates. In other words, we neglect all transverse derivatives in Eqs. (25) and (26) to obtain

$$\left[1 + \frac{\alpha}{2}\sin^2(\vartheta)\right]\frac{\partial}{\partial t_f}\binom{f}{b} \pm \frac{\partial}{\partial z}\binom{f}{b} = \mp\frac{\alpha}{4}\sin(2\vartheta)\frac{\partial\vartheta}{\partial z}\binom{f}{b}, \qquad (34)$$

$$\frac{\partial\vartheta}{\partial t_\ell} = \frac{\partial^2\vartheta}{\partial z^2} + \sin(2\vartheta)\langle|f|^2 + |b|^2\rangle_{t_f}, \qquad (35)$$

where we have used z to indicate x_3'. The boundary conditions are

$$f(0,t_f) = R_L B(0,t_f) + f_{in}, \qquad (36)$$

$$b(1,t_f) = R_R e^{i\psi} f(1,t_f), \qquad (37)$$

$$\vartheta(0,t_\ell) = \vartheta_L, \quad \vartheta(1,t_\ell) = \vartheta_R. \qquad (38)$$

We now show that the only asymptotic solution of Eqs. (34) is time stationary. This result is suggested by the physics of the problem: a field evolving in a linear cavity, albeit with a complicated refractive index. Any initial transient dies after a sufficiently large number of reflections from the (leaky) cavity mirrors and the cavity settles down in a stationary equilibrium configuration. More formally, taking the Laplace transform of Eqs. (34), (36), and (37) and using the initial conditions $f(z,0) = b(z,0) = 0$ we obtain that the forward field is given by [29]

$$f(z,t) = \frac{f_{in}}{2\pi i}\int_{\gamma-i\infty}^{\gamma+i\infty}\frac{e^{st}}{s}\frac{e^{-sz-\alpha\sin^2[\vartheta(z)]/4}}{1 - Re^{-2s}e^{i\psi}}ds, \qquad (39)$$

where $R \equiv R_L R_R$ and γ is chosen so that the integration path lies to the left of all the singularities of the integrand. The integrand has a pole at $s = 0$ and countably many poles at

$$s_n = \frac{1}{2}\log(R) + i\left(\frac{\psi}{2} + n\pi\right), \quad n = 0,1,2,\ldots. \qquad (40)$$

The term in the residue expansion that corresponds to the pole at $s = 0$ is the stationary solution

$$f(z) = \frac{e^{-\alpha\sin^2(\vartheta)/4}}{1 - Re^{i\psi}}f_{in}. \qquad (41)$$

The other poles give the Fourier series expansion of the backward and forward reflection of the initial step in the boundary condition and decay exponentially fast with a decay rate determined by the losses at the mirrors. In the same manner we obtain that the asymptotic solution for the backward field is

$$b(z) = \frac{R_R e^{i\psi} e^{-\alpha\sin^2(\vartheta)/4}}{1 - Re^{i\psi}}f_{in}. \qquad (42)$$

The asymptotic solutions for the electric fields can be substituted in the director field equation (35) to obtain the plane-wave limit of equations (25) and (26):

$$\frac{\partial\vartheta}{\partial t_\ell} = \frac{\partial^2\vartheta}{\partial z^2} + |f_{in}|^2(1 + |R_R|^2)\sin(2\vartheta)\frac{e^{-\alpha\sin^2(\vartheta)/2}}{|1 - Re^{i\psi}|^2}, \qquad (43)$$

with boundary conditions $\vartheta(0,t_\ell) = \vartheta_L$ and $\vartheta(1,t_\ell) = \vartheta_R$.

B. The hybrid cavity

We now apply the model (43) to the analysis of a hybrid cavity like the one used in Ref. [15], i.e, with boundary conditions

$$\vartheta(0,t_\ell) = 0, \quad \vartheta(1,t_\ell) = \pi/2. \qquad (44)$$

The advantage of this configuration, with respect to a homeotropic one, is that there is no Fredericks transition and the director field changes smoothly under the effect of the electric field. In particular, this implies that it is possible to express the director field as a regular power expansion in the input field amplitude.

To gain some insight on the number and nature of the stationary solutions of Eq. (43) with boundary conditions (44), we introduce two approximations that allow us to obtain analytical estimates of some critical parameters involved in selecting the solutions. First we approximate

$$e^{-\alpha\sin^2(\vartheta)/2} \simeq 1. \qquad (45)$$

This is a reasonable approximation because α is assumed to be small and the argument of the exponential is in the range

$[-\alpha/2,0]$. Second, we keep only the order one term in the α-expansion of $\Delta(\vartheta)$, Eq. (22), and write the total phase shift ψ as

$$\psi = \delta_e + \frac{\alpha}{2a}\int_0^1 [\sin^2(\vartheta) - \sin^2(\vartheta_0)]dz. \qquad (46)$$

Under these assumptions we can write the time stationary version of Eq. (43) as

$$\frac{d^2\vartheta}{dz^2} + \beta \sin(2\vartheta) = 0, \qquad (47)$$

with

$$\beta = \frac{|f_{in}|^2(1+R_R^2)}{1+R^2-2R\cos(\psi)}, \qquad (48)$$

where, to make the notation lighter, we have assumed that the reflection coefficients are real.

The solution of Eq. (47), and hence, ψ, depends on β. On the other hand, from Eq. (48) we have that β depends on ψ. Therefore, the number of solutions of Eq. (47) is given by the number of intersections of the graph of $\beta(\psi)$, Eq. (48), with the graph of $\beta_\psi(\psi)$, given implicitly by Eq. (46) once we have solved Eq. (47).

Equation (47) is analogous to the pendulum equation and cannot be solved in closed form. However, we can look for a solution of Eq. (47) as a power expansion in β. This is quite successful: a comparison with the numerical solution of Eq. (43) obtained using AUTO [21,22] (see below) indicates that a third-order approximation is good even for values of β of the order of 1.

In a nutshell, these results show that the system is generically multistable and that it is easier to have multistability for negative values of the zero-field phase shift, δ_e. These results have an intuitive explanation: the effect of the intracavity field on the director field is ultimately to induce a positive phase shift proportional to the intracavity field intensity. If δ_e is negative then this positive phase shift may make the field resonant with the cavity (i.e., it induces an equivalent detuning equal to zero) and so greatly increase the intracavity field intensity. Once the field is locked in this configuration, it remains close to resonance even if the input field intensity is decreased. The same picture applies for positive δ_e, but multistability is harder to achieve because the field-induced phase shift must be large enough to cause resonance with the next longitudinal cavity mode.

Solving Eq. (47) up to third order in β and substituting into Eq. (46) we obtain that

$$\psi = \delta_e + \frac{\alpha}{2a}\left(\frac{\beta}{2\pi^2} - \frac{3\beta^3}{4\pi^6}\right) + O(\beta^5), \qquad (49)$$

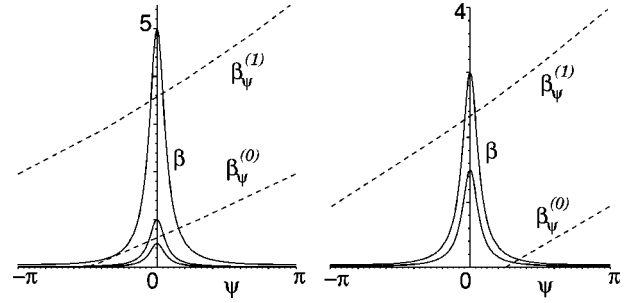which we can invert using the implicit function theorem to obtain

FIG. 2. Graphs of the functions β (solid lines) and $\beta_\psi^{(n)}$ (dashed lines) as a function of ψ for $\delta_e = -\pi/2$ (left) and $\delta_e = \pi/4$ (right). The different graphs of β correspond to $|f_{in}|^2 = \{0.01,0.05,0.1\}$ (left) and $|f_{in}|^2 = \{0.03,0.06\}$ (right) for increasing height of the graph. In this and all the following figures $\alpha = 0.1$, $a = 0.001$, and $R_L = R_R = 0.9$.

$$\beta_\psi = 4\pi^2\frac{a}{\alpha}(\psi - \delta_e) + 96\pi^2\frac{a^3}{\alpha^3}(\psi - \delta_e)^3 + O\left[\frac{a^5}{\alpha^5}(\psi - \delta_e)^5\right]. \qquad (50)$$

Equation (47) has a solution whenever β_ψ is equal to β as defined in Eq. (48). The functions β and β_ψ are defined for all real ψ. However, for representation purposes it is more convenient to restrict ψ to the range $[-\pi,\pi)$. This does not affect β because it depends on ψ only through $\cos(\psi)$. On the other hand, in order to represent all the possible values of β_ψ we must introduce a multibranched version of this function:

$$\beta_\psi^{(n)} = 4\pi^2\frac{a}{\alpha}(\psi + 2n\pi - \delta_e) + 96\pi^2\frac{a^3}{\alpha^3}(\psi + 2n\pi - \delta_e)^3$$
$$+ O\left[\frac{a^5}{\alpha^5}(\psi + 2n\pi - \delta_e)^5\right], \quad n = 0,1,2,\ldots, \qquad (51)$$

with $-\pi \le \psi < \pi$. Equation (47) has a solution whenever β is equal to any of the branches $\beta_\psi^{(n)}$.

In Fig. 2 we have plotted the graphs of β and $\beta_\psi^{(n)}$ for two values of the zero-field phase shift δ_e. Consider first the case $\delta_e > 0$ (right-hand side of Fig. 2 and bottom half of Fig. 6). For small input intensities there is only one solution and it is located in the positive ψ region. As the input intensity is increased two new solutions appear on the branch $\beta_\psi^{(1)}$ with slightly negative ψ. As the intensity is further increased one of the two new solutions moves toward positive ψ while the other has a more and more negative ψ. If the intensity is increased even further two scenarios can be envisaged. In the first, new solutions appear on higher branches of $\beta_\psi^{(n)}$. In the second, as the graph of β is shifted even more upward, the positive ψ tail of β no longer intersects $\beta_\psi^{(0)}$ while a new solution appears on $\beta_\psi^{(1)}$ with negative ψ. This then collides with the negative ψ solution already on the $\beta_\psi^{(1)}$ branch and the two disappear. This scenario happens at lower and lower intensities as δ_e gets closer and closer to π.
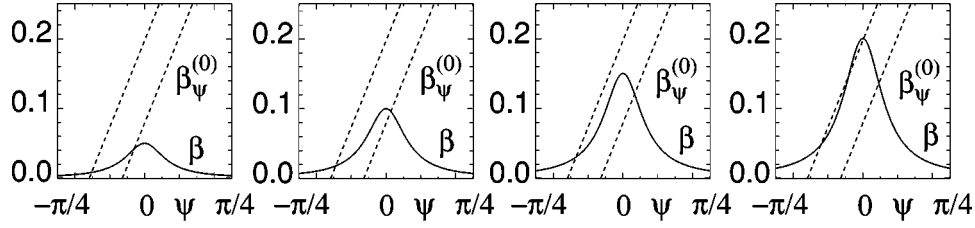
FIG. 3. Graphs of the functions β (solid lines) and $\beta_\psi^{(0)}$ (dashed lines) as a function of ψ. $|f_{in}|^2 = \{0.001, 0.002, 0.003, 0.004\}$ from left to right. In each panel, the left and right graphs of $\beta_\psi^{(0)}$ correspond to $\delta_e = \{-0.4, -0.2\}$, respectively. Note that if δ_e is too close to zero there in no bistability as the input intensity is increased.

If δ_e is negative (left-hand side of Fig. 2 and top half of Fig. 6), then for very small input field intensities there is only one solution with a value of ψ roughly equal to δ_e. As the intensity is increased two new solutions appear and the system is bistable. As the intensity is increased further one of these solutions collides with the first while the second acquires a positive value of ψ. After the collision of the two solutions with negative ψ there remains only one solution on the branch $\beta_\psi^{(0)}$, but other solutions may have already appeared on the other branches of $\beta_\psi^{(n)}$, thus making the system multistable.

Note that if δ_e is quite close to zero then the pair of solutions do not form and the single solution on the first branch of β_ψ migrates smoothly from negative to positive ψ (see Fig. 3). In fact, for the additional pair of solutions to form the graph of $\beta_\psi^{(0)}$ must be tangent to that of β. For small ψ the slope of $\beta_\psi^{(0)}$ is approximately constant as a function of ψ and given by

$$\frac{d}{d\psi}\beta_\psi^{(0)} \simeq \frac{4\pi^2 a}{\alpha}. \tag{52}$$

The slope of β, instead, is given by

$$\frac{d\beta}{d\psi} = -|f_{in}|^2 \frac{2R(1+R_R^2)\sin(\psi)}{[1+R^2-2R\cos(\psi)]^2}, \tag{53}$$

and ranges from zero to a maximum value that is proportional to $|f_{in}|^2$. As can be seen from Fig. 3 if δ_e is negative and close to zero, the graphs of β and β_ψ cross at small values of $|f_{in}|^2$, so small that the maximum slope of β is smaller than the slope of β_ψ, Eq. (52), and the tangency cannot take place. More quantitatively, to compute the upper bound on δ_e for multistability to exist, we must do the following.

(1) Find the value ψ_{max} of ψ where β has maximum slope.

(2) Impose that β and $\beta_\psi^{(0)}$ have the same slope at $\psi = \psi_{max}$ and find the corresponding value of the input intensity, I_{max}.

(3) Impose that $\beta = \beta_\psi^{(0)}$ at $\psi = \psi_{max}$ and $|f_{in}|^2 = I_{max}$ to find the corresponding value of the zero-field phase shift, δ_{max}. This is the upper bound on δ_e for multistability to occur.

We find that ψ_{max} is given by

$$\tan(\psi_{max}) = -\frac{\sqrt{2}(-1-10R^2+\sqrt{1+34R^2+R^4}-R^4+R^2\sqrt{1+34R^2+R^4})^{1/2}}{-1-R^2+\sqrt{1+34R^2+R^4}}. \tag{54}$$

The value of the input intensity where the maximum slope of β is equal to Eq. (52) is

$$I_{max} = -\frac{2\pi a}{\alpha}\frac{[1+R^2-2R\cos(\psi_{max})]^2}{R(1+R_R^2)}. \tag{55}$$

Finally, the upper bound on the zero-field phase shift for multistability to occur is

$$\delta_{max} = \psi_{max} - \frac{\alpha}{4\pi^2 a}\frac{I_{max}(1+R_R^2)}{1+R^2-2R\cos(\psi_{max})}. \tag{56}$$

As can be seen from Figs. 4 and 5, this estimate of the upper bound is in good agreement with the numerical investigation of the bistability regions of Eq. (47) and, also, Eq. (43).

These results are summarized in Fig. 4, where the number of solutions of Eq. (47), computed using Eqs. (48) and (51), is identified as a function of the input field intensity and of the zero-field phase shift. On the right of the nearly vertical curve, new solutions appear at tangencies between β and successive branches of $\beta_\psi^{(n)}$ as in the right panel of Fig. 2. On the left of this curve, new solutions appear at tangencies with the same branch of $\beta_\psi^{(n)}$ as in the rightmost panel of Fig. 3. The foot of this curve is at $\delta_e \simeq \delta_{max}$ as estimated in Eq. (56). To obtain Fig. 4 we have used the property that Eq. (47) and the equation $\beta = \beta_\psi^{(n)}$ have the same number of solutions. We
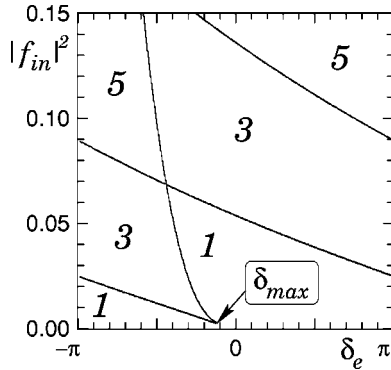
FIG. 4. Numerical multi-stability diagram of Eq. (47) in the $(\delta_e, |f_{in}|^2)$ plane: the digit inside each region indicates the number of solutions. The arrow on the horizontal axis indicates the value of δ_{max}, Eq. (56).

have, therefore, computed the function $|f_{in}|^2(\psi)$ defined by the equation $\beta = \beta_\psi^{(n)}$ for a given value of δ_e and a given branch number. We have then counted the number of folds of this function at 400 different values of $|f_{in}|^2$. This is the number of solutions of Eq. (47) for a given value of δ_e and for a given branch of $\beta_\psi^{(n)}$. We have repeated this procedure for all the branches of $\beta_\psi^{(n)}$ relevant to the plot in Fig. 4 and for 400 different values of δ_e uniformly distributed in the range $(-\pi, \pi)$.

The results discussed so far in this subsection have been obtained starting from Eq. (47). This approach has been quite fruitful, but it has two drawbacks: first of all Eq. (47) is an approximation of the stationary form of Eq. (43). Second, it gives us no information on the stability of the stationary solutions we have identified or on the existence of any time-dependent solutions of Eq. (43). In order to answer these questions we have studied numerically Eq. (43) using AUTO [21,22]. We have discretized the spatial coordinate using a Gauss-Lobatto grid [23]. This has allowed us to use a pseudo-spectral method to compute the spatial derivative of ϑ and a Gauss quadrature method [24] to compute the phase integral ψ, Eqs. (22) and (33). Sixteen grid points have proved sufficient to ensure the reliability and the accuracy of the numerical results.
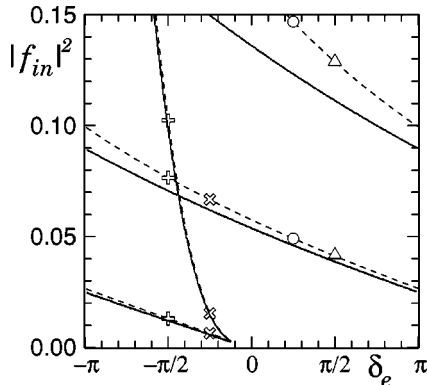

FIG. 5. Numerical multistability diagram of Eq. (43) (dashed lines) superimposed to that of Eq. (47) (solid lines). The symbols refer to the limit points in the corresponding bifurcation diagrams in Fig. 6.

Figure 5 is the equivalent for Eq. (43) of Fig. 4. The dashed lines are the boundaries between regions of multistability for Eq. (43) computed using AUTO, while the solid lines are the boundaries for Eq. (47) as in Fig. 4. As expected the agreement is quite good for low pump intensities: as the pump intensity is increased the director field changes more and more from its zero-field configuration and the approximation (46) becomes poorer and poorer. We have used AUTO also to draw in Fig. 6 the bifurcation diagram of Eq. (43) for four different values of the zero-field phase shift $\delta_e = \{-\pi/2, -\pi/4, \pi/4, \pi/2\}$ and for a large range of input intensities. To make the graphs clearer we use $|f_{in}|$ as bifurcation parameter instead of the input intensity, $|f_{in}|^2$. Note that the corresponding range of $|f_{in}|^2$ used in this figure is roughly 100 times larger than in Figs. 2–5. The graphs confirm the results of the multistability diagrams of Figs. 4 and 5. In particular, for negative values of δ_e it is possible to observe the switch from one to three and then back to one solution (see inset of the $\delta_e = -\pi/4$ diagram, top right of Fig. 6). As an aid to the eye, the limit points in each block are identified with the same symbol in Fig. 6 and Fig. 5. Moreover, form the graphs of ψ as a function of $|f_{in}|$ we can verify that new solutions appear when ψ is approximately an integer multiple of 2π, i.e., the new solutions are resonant with successive longitudinal modes of the cavity.

Figure 6 provides also information on the stability of the solutions: as expected from standard results of bifurcation theory [25] at each limit point there is a change of stability and if the system has $2n+1$ solutions then $n+1$ of these are stable and n are unstable. No bifurcation to a time-dependent solution has been detected. To clarify whether time-dependent solutions disconnected from the stationary branches may exist we have integrated numerically Eq. (43). We have used a Chebychev collocation method and a Gauss-Lobatto grid to compute the spatial derivative and a variable order variable step method [26] to integrate the resulting ordinary differential equations in time. Various simulations for a range of values of the input field intensity have been run, but in all cases the system settled on a time stationary solution.

To summarize, we have shown that in the plane-wave limit a hybrid microcavity shows multistability for both signs of the cavity detuning. The mechanisms for bistability are slightly different in the two cases and, as a consequence, it is possible to have very low power bistability only for negative values of the detuning. Moreover, the model has only time stationary solutions to which it relaxes after a fairly short transient. Another set of stationary solutions, disconnected from the zero-field solution, is discussed at the end of the following section.

C. The homeotropic cavity

The boundary conditions on the director field for a homeotropic cavity are

$$\vartheta(0, t_\ell) = 0, \quad \vartheta(1, t_\ell) = 0. \tag{57}$$

With these boundary conditions Eq. (43) admits a zero solution, $\vartheta_0(z, t_\ell) = 0$, for all values of the input field amplitude
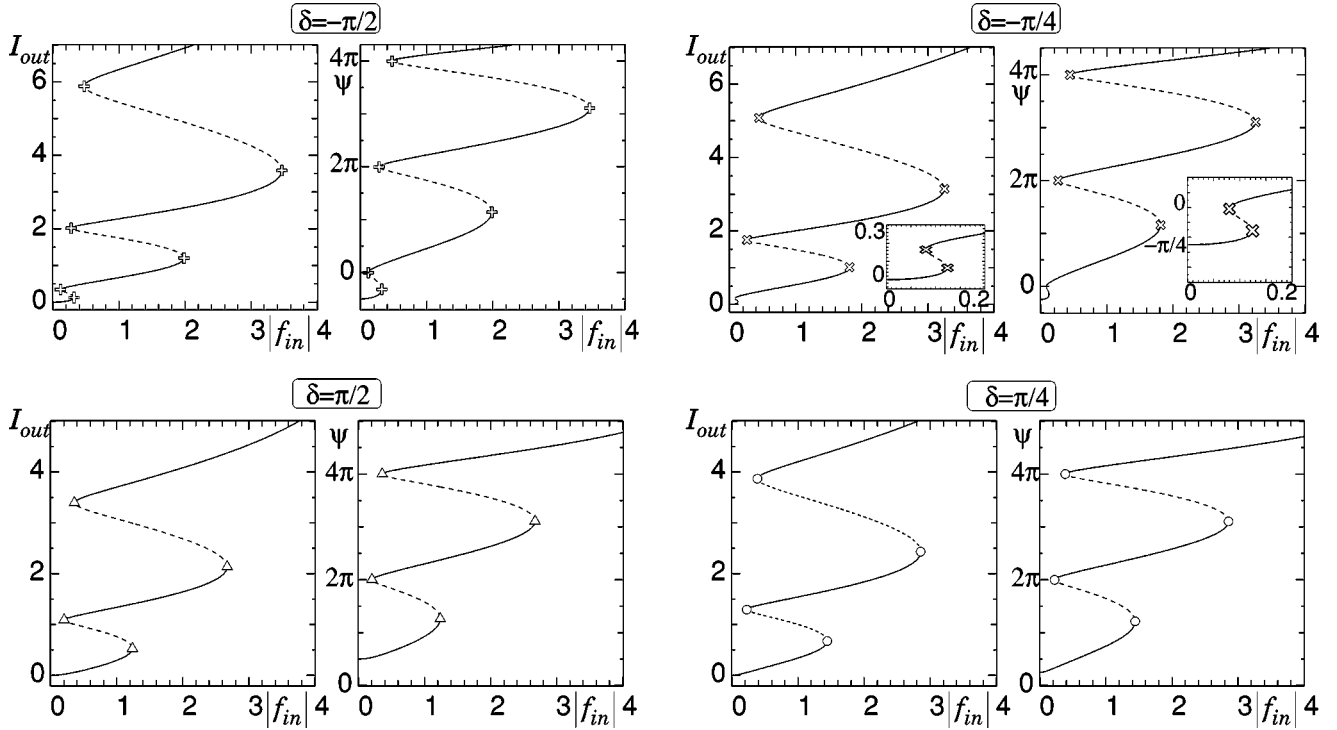
FIG. 6. Bifurcation diagrams of Eq. (43) for $\delta_e = \{-\pi/2, -\pi/4, \pi/4, \pi/2\}$ per block clockwise from top left. In all diagrams the horizontal axis is the modulus of the input pump. The vertical axis of the left (right) diagram in each block is the output intensity (total phase shift ψ). The solid (dashed) lines indicate (un)stable solutions. The symbols on the limit points correspond to those used in Fig. 5. The insets in the top right block are enlargements of the region near the origin of their respective graphs.

f_{in}. This becomes unstable for sufficiently large input field intensity and it is possible to derive an equation for the amplitude of its perturbation in a neighborhood of the bifurcation point. To simplify the notation we assume that the reflectance of the mirrors is real and write Eq. (43) as

$$\frac{\partial \vartheta}{\partial t_\ell} = \frac{\partial^2 \vartheta}{\partial z^2} + \sin(2\vartheta) \frac{|f_{in}|^2 (1+R_R^2)}{1+R^2-2R\cos(\psi)} e^{-\alpha \sin^2(\vartheta)/2}. \tag{58}$$

By linearizing Eq. (58) around the zero solution we obtain that the instability mode with lowest threshold is $\sin(\pi z)$ and that the threshold input intensity, $|f_{in}^{(0)}|^2$, is given by

$$(1+R_R^2)|f_{in}^{(0)}|^2 = \frac{\pi^2}{2}[1+R^2-2R\cos(\delta_e)]. \tag{59}$$

We define the bifurcation parameter η by

$$|f_{in}|^2 = |f_{in}^{(0)}|^2 + \eta, \quad \eta \ll 1, \tag{60}$$

and expand the director field equations in powers of η as

$$\vartheta(z,\bar{z},\bar{t},\dots) = \eta \vartheta_1(\bar{z},\bar{t},\dots)\sin(\pi z)$$

$$+ \eta^2 \sum_{n=1}^{\infty} \vartheta_{2n} \sin(n\pi z) + O(\eta^3), \tag{61}$$

where the overbar symbols refer to the order in η. For example, $\bar{z} = \eta z$. Expanding in powers of η and requiring at

each order that the appropriate solvability conditions [27] are satisfied, we obtain that the director field can be written near threshold as

$$\vartheta(z,t_\ell) = \tilde{\vartheta}(t_\ell)\sin(\pi z) + \frac{1}{48}\tilde{\vartheta}^3\sin(3\pi z) + O(\tilde{\vartheta}^4), \tag{62}$$

where up to order η^3 the amplitude $\tilde{\vartheta}(t_\ell)$ of the perturbation obeys the equation

$$\frac{d\tilde{\vartheta}}{dt_\ell} = \frac{2(1+R_R^2)(|f_{in}|^2 - |f_{in}^{(0)}|^2)}{1+R^2-2R\sin(\delta_e)}\tilde{\vartheta}$$

$$- \frac{\pi^2}{2}\left\{1 + \frac{\alpha(1-\alpha)R\sin(\delta_e)}{a[1+R^2-2R\sin(\delta_e)]}\right\}\tilde{\vartheta}^3. \tag{63}$$

In particular, we also obtain that the bifurcation is either subcritical or supercritical and that the boundary between the two regimes is given by

$$1 + \frac{\alpha(1-\alpha)R\sin(\delta_e)}{a[1+R^2-2R\sin(\delta_e)]} = 0. \tag{64}$$

The numerical value of δ_e obtained from this equation for the parameters $R_L = R_R = 0.9$, $\alpha = 0.1$ and $a = 0.001$ ($\delta_e = -0.000\,495\,2$) is in excellent agreement with the numerical estimates obtained using AUTO to draw the bifurcation diagrams of Eq. (58).
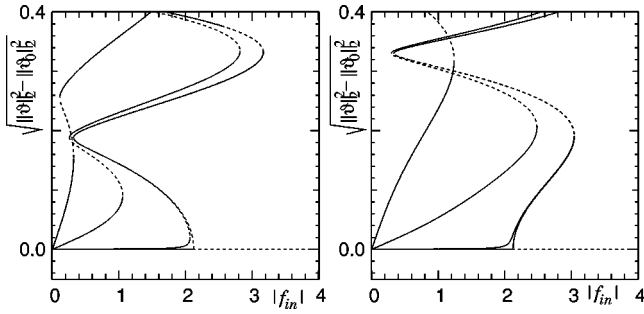
FIG. 7. Bifurcation diagram for $\delta_e = -\pi/2$ (left) and $\delta_e = \pi/2$ (right) for $\log_{10}(\epsilon) = \{0, -1, -3, -9\}$ from left to right in each picture. The symbol $\|\cdot\|_2$ indicates the L_2 norm, while the symbol ϑ_0 indicates the zero electric field stationary solution of the director field equation (58). The solid (dashed) lines refer to (un)stable solutions. The values of the other parameters are $\alpha = 0.1$ and $a = 0.001$.

FIG. 9. Bifurcation diagram of Eq. (43) showing both the branch connected to the zero-field solution and the branch disconnected from it. The vertical axes on the two diagrams are the output field intensity (left) and the total phase shift ψ (right). The solid (dashed) lines refer to (un)stable solutions. The numbers refer to the solutions drawn in Fig. 10. The values of the other parameters are $\delta_e = -\pi/2$, $a = 0.001$, and $\alpha = 0.1$.

We can interpret the two different bifurcation regimes of the homeotropic case in terms of the bifurcation diagrams for the hybrid case. In Fig. 7 we have drawn the numerical bifurcation diagram of Eq. (58) with boundary conditions

$$\vartheta(0, t_\ell) = 0, \quad \vartheta(1, t_\ell) = \epsilon \pi/2, \qquad (65)$$

for different values of ϵ: $\epsilon = 1$ corresponds to the hybrid cavity while $\epsilon = 0$ corresponds to the homeotropic cavity. We can see that for $\delta_e = -\pi/2$ the bifurcation diagram of the hybrid cavity is smoothly changed into the subcritical bifurcation of the homeotropic cavity (left-hand panel of Fig. 7). For $\delta_e = \pi/2$, instead, the change is to a supercritical bifurcation.

Conversely, the bifurcation diagram of the homeotropic cavity gives the possibility of detecting solutions of the hybrid cavity that are not connected to the zero electric field solution. With suitable scaling we can write Eq. (63) in supercritical regime as the normal form

$$\dot{x} = \mu x - x^3, \qquad (66)$$

where μ is the bifurcation parameter and x is a generic variable. A generic perturbation of this normal form transforms it into (p. 276 of Ref. [28])
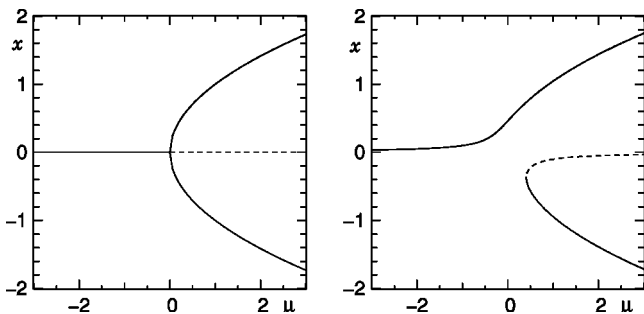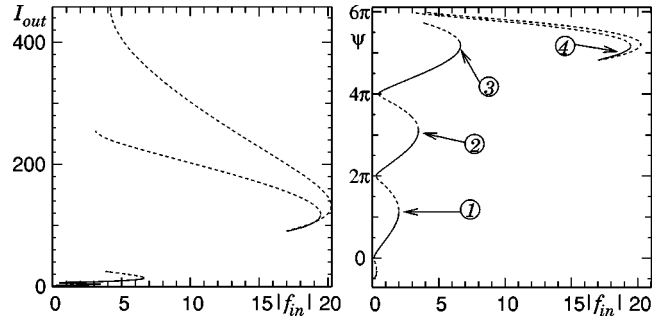
$$\dot{x} = \nu + \mu x - x^3 \qquad (67)$$

and the bifurcation diagram is altered quite dramatically as can be seen in Fig. 8: the pitchfork bifurcation point disappears and the lower and upper branches become disconnected.

We can expect that a nonzero boundary condition on the right-hand side of the cavity, i.e., $\epsilon \neq 0$ in Eq. (65), will give rise to a nonzero constant term in Eq. (63) and transform it in a form similar to Eq. (67). In this case, a disconnected branch of solutions will appear: the director field becomes negative in a neighborhood of the left-hand boundary and then switches to positive values as it gets closer to the right mirror so as to satisfy the boundary condition there. This is indeed the case: we have used AUTO to track the negative ϑ branch from $\epsilon = 0$ to $\epsilon = 1$. We have then drawn a complete bifurcation diagram for $\epsilon = 1$ (hybrid cavity, see Fig. 9) and calculated solutions of the director field equation both on the branch that is connected to the zero-field solution and on the one disconnected from it (see Fig. 10). As can be seen from Fig. 9 the disconnected solution is stable, albeit in a small region of parameter space. However, its basin of attraction

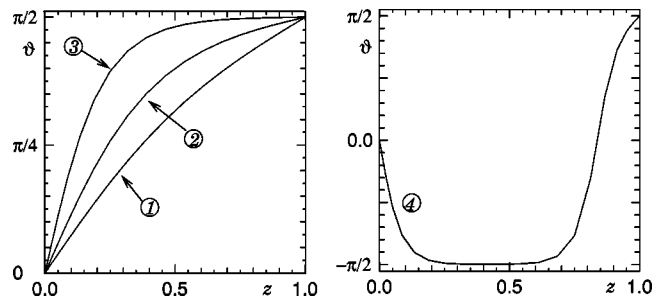FIG. 8. Bifurcation diagram of Eq. (66), left, and Eq. (67), right. $\nu = 0.1$ in the right panel.

FIG. 10. Graphs of the director field as a function of the coordinate along the cavity. The graphs on the left-hand side correspond to three different solutions on the connected branch (points 1,2,3 in Fig. 9, $|f_{in}| = \{1.99, 3.47, 6.63\}$, respectively, from 1 to 3). The graph on the right-hand side is a stable solution on the disconnected branch corresponding to $|f_{in}| = 18.667$, point 4 in Fig. 9.

may be small and it may not be trivial to make the system choose this configuration instead of the solution connected to zero.

IV. CONCLUSIONS

We have derived and analyzed a model of a liquid crystal filled microcavity, i.e., a cavity whose length is only a few hundred wavelengths. We would like to conclude by discussing how the model ought to be modified if the length of the cavity is outside this range. This parameter appears twice in the derivation of the model: when making the slowly varying amplitude approximation and when choosing the scaling in the definition of the nondimensional variables.

The slowly varying amplitude approximation requires the electric field amplitude and the director field to vary on a length scale much longer that the light wavelength. This approximation is clearly untenable if the length of the cavity itself is only a few wavelengths. In this case, Maxwell's wave equation (5) cannot be simplified using the slowly varying amplitude approximation. A possible method of analysis is to consider only the time stationary case, the approach of Refs. [6,7]. Another possibility is to focus on the propagation of a single cavity mode, an approach similar to that of Ref. [10]. However, even though the model (43) is not valid for very short cavities, some of its properties still hold in this limit. In particular, the scaling of the electric field, Eq. (23), is proportional to the length of the cavity: as a consequence, as the cavity gets shorter a higher and higher input pump power is required to observe bistability. This is to be expected since the frequency spacing between longitudinal modes increases with decreasing cavity length and mode hopping becomes, as a consequence, harder.

If the cavity is more than a few orders of magnitude longer than the light wavelength (but still short enough for scattering from the liquid crystal not to extinguish the field),

then the model should be slightly modified. The choice of scaling in the definition of the nondimensional transverse coordinates, Eq. (20), is dictated by the fact that the width of a spot whose Rayleigh length is equal to the length of the cavity is of the order of a few wavelengths. Therefore, diffraction is not the dominant factor in selecting the size of the transverse pattern and the transverse diffusion of the liquid crystal is the main constraint on the size of the patterns. At the same time, the liquid crystal molecules are forced to change direction from 0 to $\pi/2$ in a short distance and, as a consequence, are rather "stiff." As the cavity length increases, these statements lose their validity: diffraction begins to dominate over diffusion and the liquid crystal molecules in the bulk feel only weakly the constraints imposed on the boundaries of the cavity. Equations (25) and (26) remain valid in the long cavity limit, but it is more appropriate to scale the transverse coordinates with Ref. [20] $L_T \equiv \sqrt{\pi/\lambda L}$, where λ is the light wavelength. Moreover, the liquid crystal time scale τ_ℓ should be defined as the time taken by the rotation to diffuse over a distance L_T. With this scaling the transverse Laplacian in Eqs. (25) and (26) has coefficient equal to one, while the coefficient of the second derivative of the director field in the longitudinal direction tends to zero as the length of the cavity increases to infinity, reflecting the ever decreasing relevance of the longitudinal elastic restorative force.

ACKNOWLEDGMENTS

[1] G. Abbate and J.M. Otón, Adv. Mater. **12**, 459 (2000).

[2] E. Braun, L.P. Faucheux, and A. Libchaber, Phys. Rev. A **48**, 611 (1993).

[3] J.F. Henninot, M. Debailleul, F. Derrien, G. Abbate, and M. Warenghem, Synth. Met. **124**, 9 (2001).

[4] M. Peccianti, A. De Rossi, G. Assanto, A. De Luca, C. Umeton, and I.C. Khoo, Appl. Phys. Lett. **77**, 7 (2000).

[5] M. Peccianti and G. Assanto, Phys. Rev. E **65**, 035603(R) (2002).

[6] D.W. McLaughlin, D.J. Muraki, and M.J. Shelley, Physica D **68**, 116 (1993).

[7] D.W. McLaughlin, D.J. Muraki, and M.J. Shelley, Physica D **97**, 471 (1996).

[8] J.A. Reyes and P. Palffy-Muhoray, Phys. Rev. E **58**, 5855 (1998).

[9] J.A. Reyes and R.F. Rodrigues, Physica D **141**, 333 (2000).

[10] C. García-Reimbert, C. Garza-Hume, A.A. Minzoni, J.A. Reyes, R.F. Rodríguez, and N.F. Smyth, Physica D **145**, 144 (2000).

[11] N.V. Tabiryan, S.R. Nersisyan, and M. Warengehm, Phys. Rev. Lett. **77**, 3355 (1996).

[12] M. Cheung, S.D. Durbin, and Y.R. Shen, Opt. Lett. **8**, 39 (1983).

[13] H.M. Gibbs, S.L. McCall, and T.N.C. Venkatcsan, Phys. Rev. Lett. **36**, 1135 (1976).

[14] J.V. Moloney and H.M. Gibbs, Phys. Rev. Lett. **48**, 1607 (1982).

[15] S. Hoogland, J.J. Baumberg, S. Coyle, J. Baggett, M.J. Coles, and H.J. Coles, Phys. Rev. A **66**, 055801 (2002).

[16] P.Y. Wang, J.H. Dai, and H.J. Zhang, Phys. Rev. A **41**, 3250 (1990).

[17] P.Y. Wang, W. Lu, D. Yu, and R.G. Harrison, Opt. Commun. **189**, 127 (2001).

[18] J.D. Jackson, *Classical Electrodynamics*, 3rd ed. (Wiley, New York, 1999).

[19] P.G. de Gennes and J. Prost, *The Physics of Liquid Crystals*, 2nd ed. (Clarendon Press, Oxford, 1993).

[20] L.A. Lugiato, G.-L. Oppo, J.R. Tredicce, L.M. Narducci, and

M.A. Pernigo, J. Opt. Soc. Am. B **7**, 1019 (1990).

[21] E.J. Doedel, H.B. Keller, and J.P. Kernévez, Int. J. Bifurcation Chaos Appl. Sci. Eng. **1**, 493 (1991).

[22] E.J. Doedel, H.B. Keller, and J.P. Kernévez, Int. J. Bifurcation Chaos Appl. Sci. Eng. **1**, 745 (1991).

[23] C. Canuto, M.Y. Hussaini, A. Quarteroni, and T.A. Zang, *Spectral Methods in Fluid Dynamics* (Springer-Verlag, New York, 1988).

[24] W.H. Press, S.A. Teukolsky, W.T. Vetterling, and B.P. Flannery, *Numerical Recipes in Fortran*, 2nd ed. (Cambridge University Press, Cambridge, 1992).

[25] J. Guckenheimer and P.J. Holmes, *Nonlinear Oscillations, Dynamical Systems and Bifurcations of Vector Fields* (Springer-Verlag, New York, 1983).

[26] URL: http://www.netlib.org

[27] P. Manneville, *Dissipative Structures and Weak Turbulence* (Academic Press, Boston, 1990).

[28] P. Glendinning, *Stability, Instability and Chaos* (Cambridge University Press, Cambridge, 1994).

[29] In deriving this expression we have neglected the coefficient in front of the time derivative. This choice does not invalidate the main results of this paragraph, i.e., that there is only one asymptotic solution, that this is stationary and given by Eqs. (41) and (42). On the other hand, it makes the notation much lighter and, hopefully, the line of reasoning clearer.